Inorganic Chemistry

Article

pubs.acs.org/IC

Synergistic Effects of Intrinsic Cation Disorder and Electron-Deficient Substitution on Ion and Electron Conductivity in $La_{1-x}Sr_xCo_{0.5}Mn_{0.5}O_{3-\delta}$ (x = 0, 0.5, and 0.75)

Junling Meng,[†,‡] Na Yuan,[†,§,⊥] Xiaojuan Liu,[*,†] Chuangang Yao,[†,‡] Qingshuang Liang,[†,‡] Defeng Zhou,[§] Fanzhi Meng,[*,†] and Jian Meng[†]

[†]State Key Laboratory of Rare Earth Resource Utilization, Changchun Institute of Applied Chemistry, Chinese Academy of Sciences, Changchun 130022, P. R. China

[‡]University of Chinese Academy of Sciences, Beijing 100049, P. R. China

[§]School of Chemistry and Life Science, Changchun University of Technology, Changchun 130012, P. R. China

S *Supporting Information*

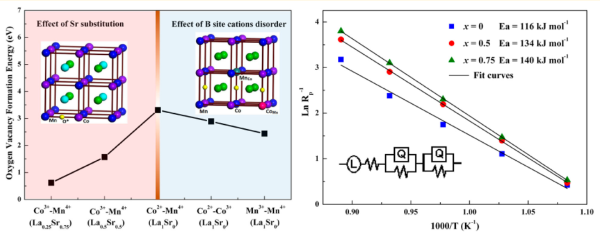

ABSTRACT: The effects of intrinsic cation disorder and electron-deficient substitution for $La_{1-x}Sr_xCo_{0.5}Mn_{0.5}O_{3-\delta}$ (LSCM, x = 0, 0.5, and 0.75) on oxygen vacancy formation, and their influence on the electrochemical properties, were revealed through a combination of computer simulation and experimental study. First-principles calculations were first performed and found that the tendency of the oxygen vacancy formation energy was Mn^{3+}-O*-Mn^{4+} < Co^{2+}-O*-Co^{3+} < Co^{2+}-O*-Mn^{4+}, meaning that antisite defects not only facilitate the formation of oxygen vacancy but introduce the mixed-valent transition-metal pairs for high electrical conductivity. Detailed partial density of states (PDOS) analysis for Mn on Co sites (Mn_{Co}) and Co on Mn sites (Co_{Mn}) indicate that Co^{2+} is prone to being Co^{3+} while Mn^{4+} is prone to being Mn^{3+} when they are on antisites, respectively. Also it was found that the holes introduced by Sr tend to enter the Co sublattice for x = 0.5 and then the O sublattice when x = 0.75, which further promotes oxygen vacancy formation, and these results are confirmed by both the calculated PDOS results and charge-density difference. On the basis of microscopic predictions, we intentionally synthesized a series of pure LSCM compounds and carried out comprehensive characterization. The crystal structures and their stability were characterized via powder X-ray Rietveld refinements and in situ high-temperature X-ray diffraction. X-ray photoelectron spectroscopy testified to the mixed oxidation states of Co^{2+}/Co^{3+} and Mn^{3+}/Mn^{4+}. The thermal expansion coefficients were found to match the $Ce_{0.8}Sm_{0.2}O_{2-\delta}$ electrolyte well. The electrical conductivities were about 41.4, 140.5, and 204.2 S cm^{-1} at doping levels of x = 0, 0.5, and 0.75, and the corresponding impedances were 0.041, 0.027, and 0.022 Ω cm^2 at 850 °C, respectively. All of the measured results testify that Sr-doped $LaCo_{0.5}Mn_{0.5}O_3$ compounds are promising cathode materials for intermediate-temperature solid oxide fuel cells.

1. INTRODUCTION

Developing clean, environmentally friendly energy technology to promote economic development and benefit future generations sequentially is one of the critical scientific challenges for contemporary researchers. Solid oxide fuel cell (SOFC) technology has been regarded as a promising route for the clean and efficient production of electricity.[1,2] Nevertheless, the prohibitive cost and scarcity of noble-metal catalysts limit the practical application of this electrochemical technology.[3] Researchers take advantage of the flexibility of the physical−chemical and catalytic properties of the perovskite family (ABO_3), where A and B sites can allow partial substitution to form $AA'BB'O_3$.[4,5] Recently, great efforts have been devoted to the development of mixed ion and electron conductors (MIECs) within perovskite oxides that are capable of running at intermediate temperatures and keeping the electrochemical performance as good as that in the high-temperature region.[6,7] In particular, partial antisite defects (ADs) are usually inevitable within perovskites, and it is believed that ADs have a profound effect on the physical properties.[8−10] Simultaneously, electron-deficient substitution (such as the substitution here of Sr^{2+} for La^{3+}) is a ready route to promoting electron and ion conductivity. Undoubtedly, both the ionic and electrical conductivities should be strongly influenced by the degree of ADs and electron-deficient substitution.

Recent computational and experimental studies have attempted to develop new fundamental descriptors of oxygen vacancy formation for the design of efficient SOFC cathode materials. Key descriptors include the oxide enthalpy of formation and the minimum band-gap energy, which exactly correspond to the metal−oxygen bond strengths and the energy of the oxygen vacancy electron density redistribution.[11] On the basis of these results, it has been recommended that the

Received: December 15, 2014
Published: March 2, 2015

ACS Publications

DOI: 10.1021/ic502989c
Inorg. Chem. 2015, 54, 2820−2829

targeted oxygen vacancy energies could be obtained by consideration of the bond strengths and electronic structures of the constituent oxides. For instance, by a combination of the intermediate bond strength of $La_{1-x}Sr_xCo_{0.5}Mn_{0.5}O_{3-\delta}$ (LSCM, x = 0, 0.5, and 0.75) and the low bond strength of $La_{1-x}Sr_xCoO_3$ (LSC) and/or $La_{1-x}Sr_xNiO_3$ (LSN), an optimal value for solar thermochemical fuel production cycles could be attained. To the best of our knowledge, the most thoroughly studied perovskite-type cathode materials are $Sr_2Fe_{2-x}Mo_xO_6$ (SFMO). It was first proposed as a promising MIEC material by Kobayashi et al. in 1998.[12] Theoretically, Carter's group investigated the AD effect on the oxygen vacancy formation in SFMO; they found that the formation energy for oxygen vacancies along the M−O−M′ bonds follow the trend Fe−O−Fe < Fe−O−Mo < Mo−O−Mn, which indicates that oxygen diffusion should be enhanced for local higher concentrations of Fe, highlighting Fe-rich SFMO-based materials.[10] Simultaneously, Chen et al. experimentally testified that Fe-rich $Sr_2Fe_{1.5}Mo_{0.5}O_6$ shows high electrical conductivity in both air and hydrogen environments, excellent redox stability, and promising performance as electrodes in symmetrical SOFC.[13] Later, by joint experimental and theoretical methods, the high concentration of constitutional oxygen vacancies is attributed to relatively weak Fe−O bonds and a fully delocalized rearrangement of the electrons left behind by the oxygen vacancy. Lastly, it was suggested that perovskites with late transition metals to weaken the transition metal−oxygen bonds and to enhance metal d−O p hybridization should be promising cathode materials for intermediate-temperature solid oxide fuel cells (IT-SOFCs).[14] Within this context, here we propose LSCM as a promising MIEC material. La_2CoMnO_6 (LCMO) initially attracted significant scientific attention for its ferromagnetic semiconductor with high critical temperature ($T_c \approx 230$ K).[15] In addition, because of the small size differences of both radii ($Co^{2+} \approx 1.302$ Å vs $Mn^{4+} \approx 1.323$ Å) and the covalent states (2+) between Co^{2+} and Mn^{4+} within the B sublattice, Co/Mn disordering is expected, which will have a strong influence on the ionic conductivity. In the meantime, electron-deficient substitution has been explicitly identified to promote oxygen diffusion in the simple perovskite $La_{1-x}Sr_xFeO_{3-\delta}$ (x = 0, 0.25, and 0.50).[16] An important motivating point for this paper is the lack of understanding of how the thus-far inevitable cation disorder and electron-deficient substitution affect the electrochemical property in LSCM. Our motivation in this paper is to answer the following three questions by using joint experimental and theoretical efforts: one is, what is the influence of Co/Mn cation disorder on the ionic conductivity? Another point is, how does electron-deficient substitution affect the oxygen vacancy formation? Finally, how good is this series of compounds as cathode materials in reality?

2. EXPERIMENTAL SECTION

Computation. All calculations reported in this work were carried out using the *VASP* code (version 5.2.2).[17] The nuclei and core electrons were represented within the frozen-core projector-augmented wave approach[18] using standard potentials for Co ($4s^23d^7$), Mn ($4s^23d^5$), La ($5s^25p^66s^25d^1$), Sr ($4s^24p^65s^2$), and regular O ($2s^22p^4$) from the *VASP* library, where the outer core/valence electrons shown in parentheses are self-consistently optimized.[19] Electron exchange and correlation was evaluated within the generalized gradient approximation using the functional of Perdew, Burke, and Ernzerhof (PBE).[20] A semiempirical effective Hubbard parameter ($U_{eff} = U - J$, where U and J are the strength of Coulomb repulsion and on-site exchange interaction, respectively) is employed. In our calculations, a series of U_{eff} values (0.0−4.0 eV for Mn and 0.0−6.0 eV for Co) were testified to, and we finally selected 3.0 eV for Mn and 5.0 eV for Co according to the calculated magnetic moments and band-gap values for LCMO. A 6 × 6 × 5 Monkhorst−Pack[21] *k*-point mesh was applied to unit cell calculations and a 3 × 3 × 5 Monkhorst−Pack *k*-point for supercells. The plane-wave basis set was converged at a kinetic energy cutoff of 500 eV. Integration over the first Brillouin zone (BZ) used Gaussian smearing (σ = 0.1 eV) during structural relaxation. The tetrahedron method with Blöchl corrections[22] for BZ integration was used after geometry optimization to obtain partial density of states (PDOS), refined energies, and the final charge density for Bader analysis.[23,24] Total energies were converged to within 1 meV per formula unit.

Synthesis and Characterization Techniques. Polycrystalline powders of the LSCM series were synthesized by a modified Pechini method.[25] La_2O_3, $Sr(NO_3)_2$, $Co(NO_3)_2 \cdot 6H_2O$, and $Mn(CH_3COO)_2 \cdot 4H_2O$ were used as the starting materials and citric acid and poly(ethylene glycol) as the chelating agents. La_2O_3 was precalcined at 1000 °C for 10 h to eliminate possible carbonate and moisture and then dissolved in nitrate acid. Stoichiometric quantities of the other raw materials were dissolved in the above clear solution under conditions of constant heat and vigorous stirring. Citric acid was subsequently added in a 1:1 molar ratio of citric acid to metal ions. An appropriate amount of poly(ethylene glycol) was then dissolved in the above clear pink aqua. Subsequently, the solution was transferred to the pottery-evaporating wares and slowly vaporized in the water bath at 85 °C overnight. Black flours were obtained, followed by heating of the dry gel on the hot plate. The obtained precursor powders were first burnt at 900 °C in air for 24 h to eliminate the organic matter. The calcined powders were pelletized and annealed at 1100 °C in air for 20 h, and this process was repeated two times with intermittent grinding to form a pure phase. A $Ce_{0.8}Sm_{0.2}O_{2-\delta}$ (SDC) electrolyte powder was prepared by a soft-chemistry procedure as described elsewhere.[26]

The crystal structures of the as-prepared samples were characterized by powder X-ray diffraction (XRD) on a Rigaku D/max-2500 diffractometer (40 kV, 200 mA) with Cu Kα radiation (λ = 1.5418 Å) and employed a step scan rate of 0.02° in the 2θ range of 10−120°. Rietveld refinement data were acquired using *GSAS-EXPGUI* software.[27] An in situ high-temperature XRD study was performed using a D8 Advance diffractometer (Bruker) with Cu Kα radiation in the temperature range of room temperature (RT) to 700 °C. High-resolution field-emission scanning electron microscopy (SEM; Hitachi S-4800) along with an energy-dispersive X-ray spectrometry (EDS; XP30, Philips) was used to obtain the micrographs and chemical composition of the sintered pellets. X-ray photoelectron spectroscopy (XPS) data were collected on a VG ESCALAB 250 electron spectrometer with monochromatic Al Kα (1486.6 eV) at 12 kV and 20 mA, and all binding energies were referred to the C 1s peak (284.6 eV). A superconducting quantum interference device based magnetic property measurement system (SQUID-MPMS) was employed to investigate the effect of an applied magnetic field on magnetic moments at 5 and 300 K (M−H).

Measurement of the thermal expansion coefficients (TECs) and electrical conductivity required dense ceramic pellets to be fully mixed with a few drops of a poly(vinyl alcohol) solution, followed by dry pressing at 40 MPa and then isostatic cool pressing under 270 MPa, and then fired at 1200 °C for 24 h at a ramping rate of 1 °C min^{-1}. The relative density of sintered pellets could achieve ∼95%, which was determined by the Archimedes method. The thermal expansion study of the dense ceramic samples, which was measured on rectangular bars (∼5 mm × 5 mm × 25 mm), was performed on a NETZSCH DIL 402C apparatus from RT to 900 °C in flowing air. The electrical conductivity was measured using a Keithley 2400 sourcemeter (Keithley Instruments, Inc.) by the Van der Pauw four-probe direct-current (dc) method in the temperature range from 850 to 200 °C with an interval of 50 °C in air. Silver wire and silver paste were used to make the four probes. The measured conductivity can be corrected with the following equation:[28]

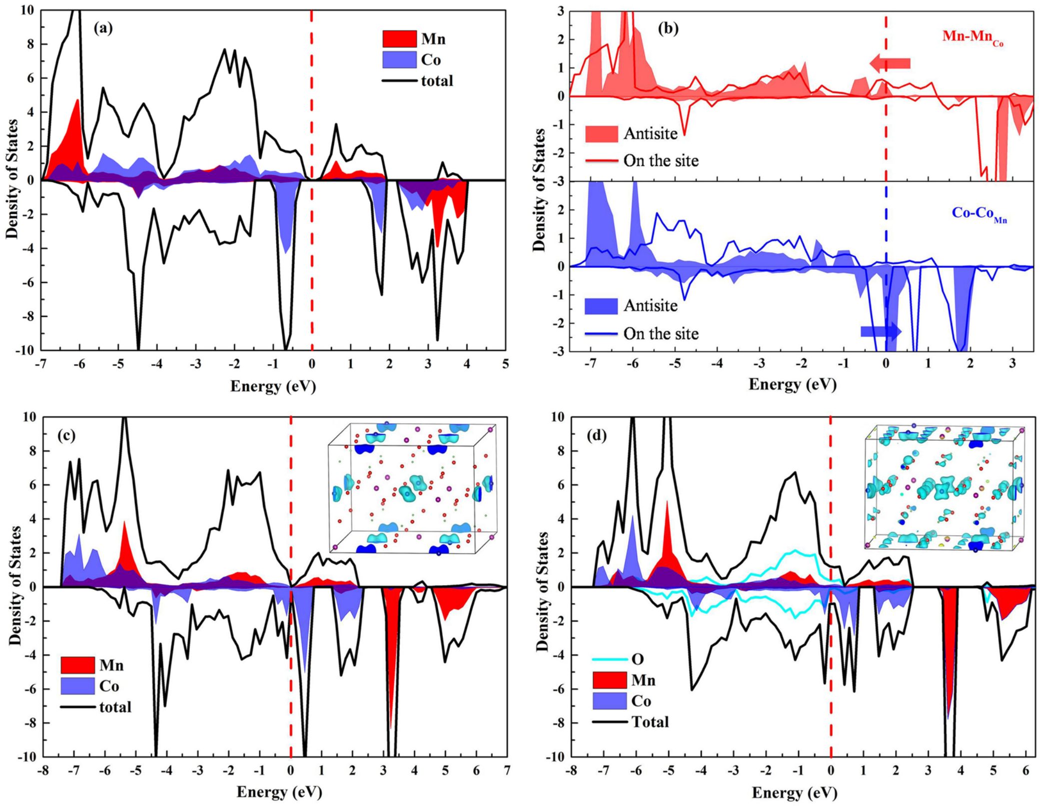

Figure 1. (a) Calculated total density of states (TDOS) and PDOS of Mn 3d and Co 3d in LCMO. (b) Comparison of Mn 3d and Co 3d PDOS at normal sites (line) and antisites (shadowed). (c) TDOS and PDOS of Co 3d and Mn 3d for Sr doping at $x = 0.5$ induced hole injection on Co [the inset is the corresponding isosurface charge-density differences (e bohr^{-3})]. (d) TDOS and PDOS of Mn 3d, Co 3d, and O 2p for Sr doping at $x = 0.75$ induced hole injection on Co and O sublattices [the inset is the corresponding isosurface charge-density differences (e bohr^{-3})]. The dashed lines present the Fermi levels.

$$\sigma_{\mathrm{corr}} = \frac{\sigma_{\mathrm{app}}}{2(d_{\mathrm{rel}}/100 - 0.5)} \qquad (1)$$

where σ_{corr}, σ_{rel}, and σ_{app} are the porosity-corrected conductivity, relative density, and measured apparent conductivity, respectively.

Symmetrical cells with a LSCM|SDC|LSCM configuration were fabricated by a screen-printing technique for electrochemical testing. Dense SDC pellets (15 mm diameter and 500 μm thickness) were prepared by pressing the powders under 40 MPa, followed by isostatic cool pressing under 270 MPa and finally sintering at 1400 °C for 10 h. LSCM cathode slurries were made by mixing the powders with binder (α-terpineol and ethylene cellulose), coated on both surfaces of SDC by screen-printing, and then fired at 1100 °C in air. The resulting electrode had a thickness of ~20 μm and an effective area of 0.25 cm^2. Silver paste was painted on both sides as a current collector, which was heated to 600 °C for 30 min in air. Electrochemical impedance spectra were collected on an Autolab Electrochemical Instruments PGSTAT302 from 850 to 650 °C in steps of 50 °C. The applied frequency range was from 1 MHz to 0.1 Hz with an amplitude signal of 10 mV under open-circuit voltage conditions.

3. RESULTS AND DISCUSSION

First-Principles Calculation Results. Absorption and diffusion of oxygen anions are mandatory capabilities for effective SOFC cathode materials. Oxygen anions are too large to diffuse in the interstices of the lattice, so oxygen vacancies (V_{O*}) in the lattice must be introduced in order for diffusion of such anions to occur (so that they may hop between empty sites). Consequently, the cost to form an oxygen vacancy is always first being considered to estimate how good a material could be as an ionic conductor.

For the perfect LCMO with space group $P2_1/n$, we correctly obtained its semiconductor property at the PBE+U level, as shown in Figure 1a, under consideration of ferromagnetic coupling between Co^{2+} and Mn^{4+}, which is also consistent with our previous relevant results.[29] By removing one neutral O atom from a $La_{16}Co_8Mn_8O_{48}$ supercell, we theoretically explored the LCMO lattice with oxygen vacancy concentrations of $\delta = 0.125$ (as represented in Figure S1 in the Supporting Information, SI), which is very close to the average experimental value of $\delta = 0.10(2)$.[14] There exist two kinds of oxygen vacancies: one is within the xy plane (O^*_{xy}), and the other is along the z direction (O^*_z). The calculated corresponding oxygen vacancy energies are 3.33 eV [$E_{\mathrm{form}}(O^*_{xy})$] and 3.29 eV [$E_{\mathrm{form}}(O^*_z)$], respectively. Thus, we employed their average value of 3.31 eV as the oxygen vacancy formation energy along Co^{2+}-O*-Mn^{4+} (shown in Figure 2, the value in the middle), which is used as a reference for the study of ADs and electron-deficient substitution effects.

Effect of Co/Mn ADs. In a $La_{16}Co_8Mn_8O_{48}$ supercell, one pair of Co/Mn are exchanged to introduce ADs; thus, the degree of ordering in the calculation is 87.5%. Previously, we found that Co^{2+} is prone to becoming Co^{3+} when it is on Mn sites, while Mn^{4+} is inclined to being Mn^{3+} when it is on Co sites,[29] which is also reproduced in the present first-principles calculation based on analysis of the Bader charges (1.29e and 1.71e for Co/Mn vs 1.52e and 1.67e for Co_{Mn}/Mn_{Co}). Also, detailed PDOS of Co and Mn 3d orbitals on both normal crystal sites and antisites are presented in Figure 1b. Obviously, compared with the PDOS of Mn 3d on the normal sites, the

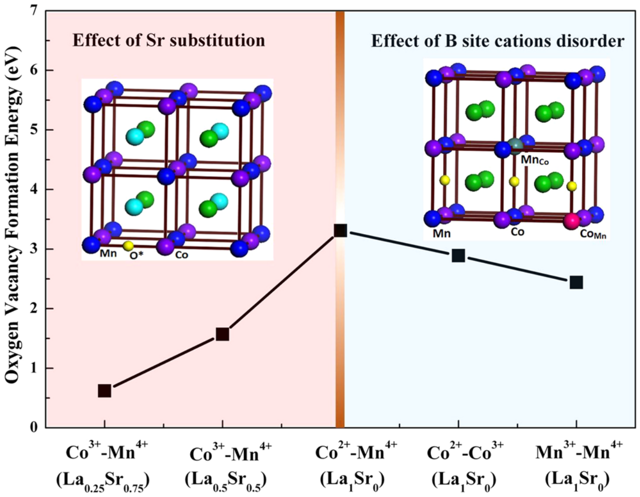

Figure 2. Theoretically predicted oxygen vacancy formation energies for LCMO, AD/LCMO, $La_{0.5}Sr_{0.5}$CMO, and $La_{0.25}Sr_{0.75}$CMO.

Mn 3d orbitals are injected electrons on the antisite, while for Co, on the contrary, electrons are lost, which is consistent with the Bader charge analysis. Thus, for LCMO with ADs, we studied also possible oxygen vacancy formation energies within Co^{2+}-O*-$Co_{Mn}{}^{3+}$ and $Mn_{Co}{}^{3+}$-O*-Mn^{4+} (ADs O*: LCMO). After removal of a neutral O atom, all supercells (with or without ADs) were given full relaxations (see Figure S1 in the SI, which depicts schematically all of the oxygen vacancies considered). The calculated average oxygen vacancy energies are shown in Figure 2 on the right. It shows the following: (1) All of the oxygen vacancy formation energies including Co^{2+}-O*-Mn^{4+} (~3.3 eV), Co^{2+}-O*-Co^{3+} (~2.73 eV), and Mn^{3+}-O*-Mn^{4+} (~2.20 eV) are lower than the ones within Sr_2FeMoO_6 (from ~3.0 to ~5.0 eV), which have been experimentally testified to be good electrode materials.[10] This result implies that LCMO (or ADs LCMO) might be a very promising cathode material and even superior to SFMO. (2) The E_{vac} tendency is Co^{2+}-O*-Mn^{4+} > Co^{2+}-O*-$Co_{Mn}{}^{3+}$ > $Mn_{Co}{}^{3+}$-O*-Mn^{4+}, meaning that oxygen vacancy forms more easily as long as the ADs exist. (3) E_{vac} of Mn-O*-Mn is further lower than that of Co^{2+}—O—Co^{3+}, demonstrating that Mn-rich LCMO-based materials should be more prospective for cathode materials with superior ionic conductivity.

Effect of Electron-Deficient Substitution. Now we address the role of Sr substitution. For this purpose, first Sr should be introduced into a La sublattice, and then all unique arrangements of La and Sr within the La sublattice should be considered. While, on the one hand, it has been found that all of these samples lack La/Sr ordering in the following powder X-ray refinement, on the other hand, for $La_{1-x}Sr_xMnO_3$, it has been theoretically found that the energies of the different La/Sr configurations at each composition (x = 0.25 and 0.50) are very close (within ~0.06 eV per formula unit), and all average structural and electronic properties are well-presented by the isotropic supercells.[30] Thus, we built the supercell models with isotropic La/Sr configurations, as shown in Figure S2 in the SI: part a represents $LaCo_{0.5}Mn_{0.5}O_{3-\delta}$, part b represents $La_{0.5}Sr_{0.5}Co_{0.5}Mn_{0.5}O_{3-\delta}$, and part c represents $La_{0.25}Sr_{0.75}Co_{0.5}Mn_{0.5}O_{3-\delta}$, with δ equal to 0.0625. To simplify, hereafter, O*: LCMO represents $LaCo_{0.5}Mn_{0.5}O_{3-\delta}$, O*: $L_{0.5}S_{0.5}$CMO represents $La_{0.5}Sr_{0.5}Co_{0.5}Mn_{0.5}O_{3-\delta}$, and O*: $L_{0.25}S_{0.75}$CMO represents $La_{0.25}Sr_{0.75}Co_{0.5}Mn_{0.5}O_{3-\delta}$. Here we emphasize the Sr doping effect on the oxygen vacancy formation energy, and the corresponding results were also shown in Figure 2 on the left. We can see that the energy of formation of the oxygen vacancy decreases with the amount of Sr, and it finally drops to only 0.62 eV in $La_{0.25}Sr_{0.75}Co_{0.5}Mn_{0.5}O_{3-\delta}$, which is significantly smaller than that of the parent LCMO, whose oxygen vacancy formation energy is about 3.31 eV. This indicates improvement of the ionic conductivity with Sr substitution. Table 1 lists the Bader charges of O*: LCMO, O*: $L_{0.5}S_{0.5}$CMO, and O*: $L_{0.25}S_{0.75}$CMO. Co-(O*) represents the Co nearest to the oxygen vacancy (O*), Mn-(O*) represents the Mn nearest to the oxygen vacancy (O*), and the corresponding charge difference analysis and PDOS for Mn 3d, Co 3d, and O 2p are shown in Figure 1c,d. We could see that the effect of Sr substitution is divided into two procedures. In the first procedure, the holes introduced by Sr mainly affect the Co sublattice, oxidizing Co^{2+} to Co^{3+} (see Figure 1c). Now the covalent difference of the cations on the B sites is only one (Co^{3+} vs Mn^{4+}); thus, it should be much easier for them to be disordering,[9] which has been found to facilitate the oxygen vacancy formation above. Finally, we conclude that with x = 0.5, on the one hand, Sr substitution makes AD formation easier in $La_{0.5}Sr_{0.5}Co_{0.5}Mn_{0.5}O_{3-\delta}$, thus decreasing the formation energy of the oxygen vacancy and increasing the ionic conductivity; on the other hand, Sr substitution itself lowers the oxygen vacancy formation energy. In the second procedure, the extra holes introduced by Sr tend to be injected into the O sublattice (see Figure 1d), making the valence of O less negative and thus making the formation of the oxygen vacancy further easier, highlighting the increase of the ionic conductivity.[31]

Table 1. Calculated Bader Charge and Magnetic Moments of $La_{1-x}Sr_xCo_{0.5}Mn_{0.5}O_{3-\delta}$ (x = 0, 0.5, and 0.75)

	LCMO	$L_{0.5}S_{0.5}$CMO	$L_{0.25}S_{0.75}$CMO
Sr concentration	0	0.5	0.75
μ_{Co}	2.46	2.89	2.88
$\mu_{Co\text{-}(O^*)}$	2.32	2.80	2.59
μ_{Mn}	3.47	3.43	3.43
$\mu_{Mn\text{-}(O^*)}$	3.78	3.51	3.56
Co	1.30	1.54	1.54
Mn	1.72	1.75	1.75
Co-(O*)	1.14	1.27	1.41
Mn-(O*)	1.51	1.62	1.63
$O_{average}$	−1.20	−1.16	−1.12
$O_{average}$-(O*)	−1.21	−1.17	−1.13

All of the calculated results above indicate three exciting points: (1) the oxygen vacancy formation energies for LCMO are all smaller than those for SFMO because both B-site ions are late transition metals with weak transition metal−oxygen bond strength; (2) because of the small covalent difference and similar sizes between Co^{2+} and Mn^{4+}, ADs should be inevitable in the synthesized compounds, while our calculated results indicate that ADs will enhance the oxygen vacancy formation; (3) Sr doping itself (electron-deficient substitution) not only lowers the oxygen vacancy formation energy but also facilitates the beneficial ADs. Obviously, ADs and electron-deficient substitution will simultaneously enhance the electrical conductivity. All of these results indicate that the LSCM series of compounds should be highly promising cathode materials.

Thus, in the following, we not only successfully synthesized this series of compounds but also performed comprehensive characterizations concerning their prospective as cathode materials for IT-SOFCs.

Structural Analysis. The RT XRD patterns of the LSCM series (Figure S3 in the SI) confirmed that every sample is a single phase within a wide 2θ range. The space group of each sample was refined using the Rietveld refinement method. We note that it is difficult to fit XRD patterns to the monoclinic structure ($P2_1/n$) because of the similarity in the X-ray scattering factors between Co and Mn; thus, the Co/Mn coordinates are constrained as equivalent within B sites.[32] For $x = 0$, the structure was refined to be orthorhombic ($\sqrt{2a_\mathrm{p}} \times 2a_\mathrm{p} \times \sqrt{2a_\mathrm{p}}$) with space group $Pnma$ (No. 62), a tetragonal structure ($a_\mathrm{p} \times a_\mathrm{p} \times 2a_\mathrm{p}$) with space group $P4/mmm$ (No. 123) was refined for $x = 0.5$, whereas the structure of the Sr-rich sample, $x = 0.75$, returned to orthorhombic with space group $Pnma$ (No. 62). It has been well-known that the perovskite oxides of Sr-doped La (such as $La_{1-x}Sr_xMnO_3$) always undergo a number of morphotropic transformations, involving rhombohedral, tetragonal, orthorhombic, or monoclinic lattice distortions. Rietveld refinement results of the LSCM series are listed in Table 2, and the refinement profiles are shown in Figure 3. All of the La and Sr ions on the A site are disorderly arranged in the LSCM series. The high R_wp parameter suggests the presence of oxygen vacancies (or interstitials) that disorder randomly within the O sublattice or the tilting orientation of BO_6 (B = Co and Mn) octahedra.[33] The pseudocubic lattice parameter (a_p) and cell volume (V) for the average perovskite structure are plotted in Figure S4 in the SI, in which a_p and V decrease so much that the diffraction peaks move to higher 2θ angles after Sr replacement (based on Bragg's law). We attributed the lattice expansion to the B-site ion reduction due to aliovalent Sr substitution.[34]

Table 2. Structural Parameters of $La_{1-x}Sr_xCo_{0.5}Mn_{0.5}O_{3-\delta}$ (x = 0, 0.5, and 0.75) Obtained from Rietveld Refinement of Powder XRD Data

	doping content		
	$x = 0$	$x = 0.5$	$x = 0.75$
space group	$Pnma$ (No. 62)	$P4/mmm$ (No. 123)	$Pnma$ (No. 62)
a (Å)	5.4831(1)	3.8445(1)	5.4605(2)
b (Å)	7.7720(2)	3.8445(1)	7.6775(2)
c (Å)	5.5241(1)	7.6900(1)	5.4261(1)
R_p (%)	7.25	7.35	7.95
R_wp (%)	11.68	9.87	10.72
χ^2	2.726	2.773	3.208

Determination of the B-site cation ordering should be characterized by neutron powder diffraction because of the different coherent scattering lengths between Co and Mn,[35] which is unfortunately not accessible for us presently. However, the saturation magnetic moments should be reduced greatly because of more Co/Mn ADs because we have known from our previous theoretical calculations that they are conversely prone to being antiferromagneitcally coupled on antisites.[29] These results could be used to indirectly demonstrate the different cation ordering degrees in these compounds. The magnetic measurement results are shown in Figure S5 in the SI. The magnetic moments $M_{5\,\mathrm{T}}$ at 5 T decreased greatly after Sr substitution (from 5.06 μ_B for $x = 0$ to 0.303 and 0.328 μ_B for $x = 0.5$ and 0.75, respectively), showing more Co/Mn ADs upon Sr substitution. We suppose that Co/Mn cation ordering is dominant for our present synthesized samples for $x = 0$, while Co/Mn becomes almost completely disordered after Sr subtitution of La with both concentrations of 0.5 and 0.75, which is consistent with not only the existing theoretical prediction but also the measured saturated magnetic moment change tendency above.

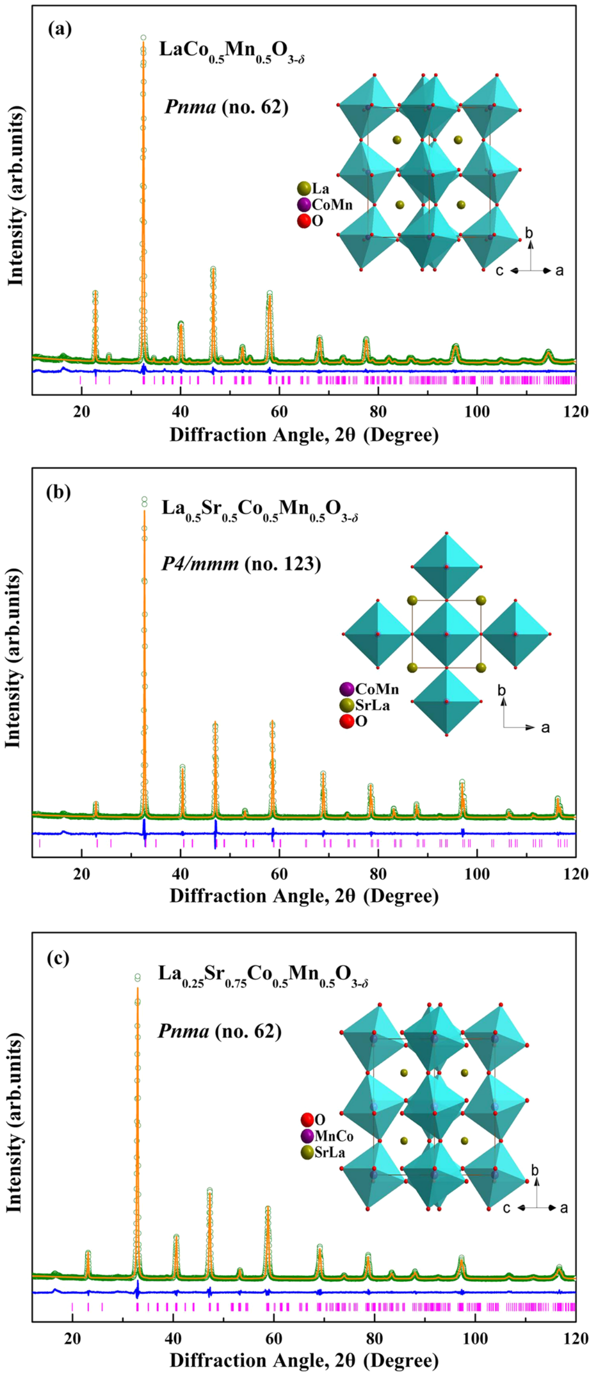

Figure 3. Rietveld refinement of powder XRD data for $La_{1-x}Sr_xCo_{0.5}Mn_{0.5}O_{3-\delta}$ (x = 0, 0.5, and 0.75). The observed (green circles), calculated (orange solid line), difference (blue line), and allowed Bragg reflection (pink vertical markers) profiles are shown.

The phase stability of electrode materials under the operation conditions is a crucial point to ensure a stable conductive performance. All of the samples were subjected to in situ high-temperature XRD examination to explore the structure stability at elevated temperatures. As shown in Figure 4, a little peak splitting for $LaCo_{0.5}Mn_{0.5}O_{3-\delta}$ at higher 2θ angles can be observed; nevertheless, such a weak change scarcely affects the whole stability. Besides, for all of the testing compounds, the crystal structures were maintained without any additional diffraction peaks being detected over the given temperature range, suggesting that the as-prepared LSCM series is stable in air up to 700 °C.

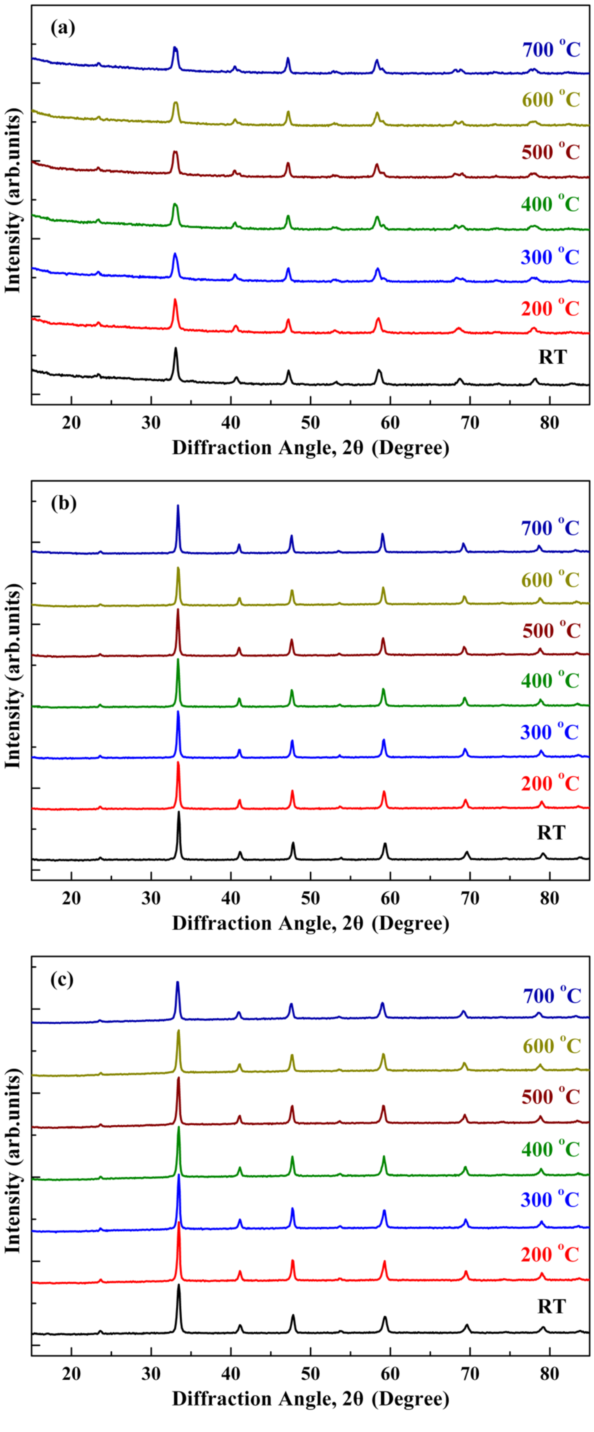

Figure 4. In situ high-temperature powder XRD of $La_{1-x}Sr_xCo_{0.5}Mn_{0.5}O_{3-\delta}$ for (a) x = 0, (b) x = 0.5, and (c) x = 0.75 over the temperature range from RT to 700 °C.

XPS Analysis. The mixed-valent Co^{2+}/Co^{3+} and Mn^{3+}/Mn^{4+} coupling on B sites plays a vital role on the electrochemical characteristics of the LSCM system. XPS was used to verify the chemical state of Co and Mn at RT with the fitting program *XPS PEAK 4.1*. The Co 2p and Mn 2p core-level spectra are shown in Figure 5. Each of them can be resolved into two components, namely, Co^{2+}/Co^{3+} and Mn^{3+}/Mn^{4+}. Every curve exhibits two weak Co^{2+} satellite peaks in Figure 5a at around 786−790 and 800−805 eV (characteristic of Co^{2+}).[36] The percentage contributions of the valence states and average valence states of Co and Mn are given in Table 3. Sr incorporation may result in the formation of oxygen vacancies or unusual oxidation states of cations on B sites. The calculated results show that the holes introduced by Sr mainly oxidize Co^{2+} to Co^{3+}; it seems contradictory to the XPS results that the percentage of Co^{3+} in x = 0.5 and 0.75 is less than that

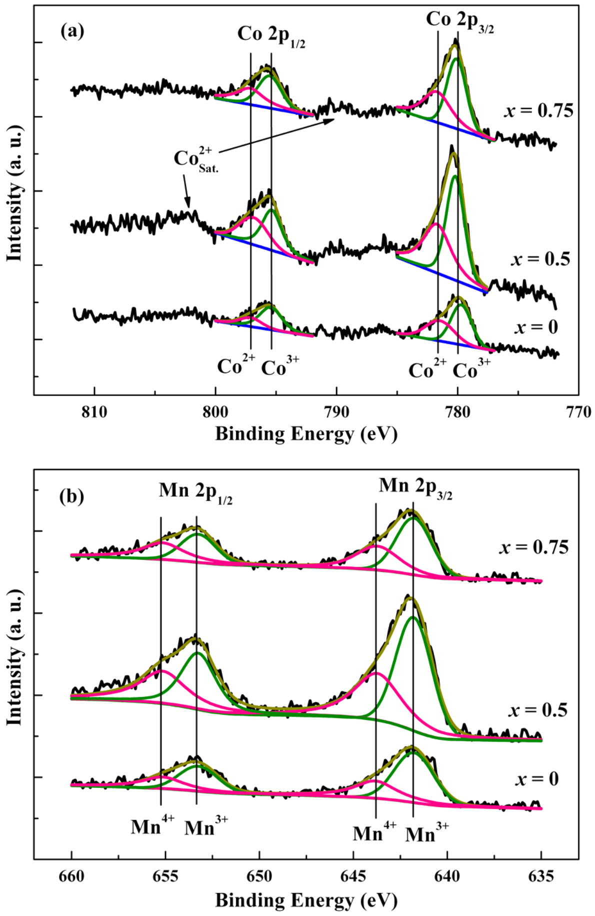

Figure 5. XPS spectra and curve fitting of the (a) Co 2p and (b) Mn 2p core levels of different Sr contents at RT.

Table 3. Proportion of Valence States and Average Valence States of Co and Mn in $La_{1-x}Sr_xCo_{0.5}Mn_{0.5}O_{3-\delta}$ (x = 0, 0.5, and 0.75)

	Co $2p_{3/2}$		Mn $2p_{3/2}$		average valence	
doping content	Co^{3+} (%)	Co^{2+} (%)	Mn^{4+} (%)	Mn^{3+} (%)	Co	Mn
x = 0	63.80	36.20	38.87	61.13	2.638	3.389
x = 0.5	54.29	45.71	45.54	54.46	2.543	3.455
x = 0.75	55.10	44.90	44.02	55.98	2.551	3.440

in $x = 0$. However, as we know for $x = 0.5$ and 0.75, a large amount of oxygen vacancies form, which will decrease the content of Co^{3+} (corresponding an increase of Co^{2+}). In the meantime, accompanied by the loss of oxygen, part of the inactive Mn^{4+} ions are reduced to Mn^{3+} because of the requirement of charge neutrality. Combined with the structure analysis above and the property test below, we can conclude that both the Mn and Co ions play vital roles in the LSCM series on the electrochemical properties. This result is consistent with the proceeding computational analysis.

Thermal Expansion and Chemical Stability. The thermal expansion behavior of the LSCM series between RT and 900 °C in air is displayed in Figure 6. The average TECs of the LSCM series (10.5×10^{-6}, 18.1×10^{-6}, and 15.2×10^{-6} K^{-1} for the samples of $x = 0$, 0.5, and 0.75, respectively) remarkably match with that of the SDC electrolyte (12.2×10^{-6} K^{-1})[37] and are much lower than that of the recently reported $Sr_2Fe_{1.5}Mo_{0.5}O_{6-\delta}$ (20.09×10^{-6} K^{-1}).[38] There are numerous factors governing the TECs, such as the spin-state transition, oxygen vacancy concentration, etc. At the lower Sr-doping level ($0 \leq x \leq 0.5$), the TECs increase with increasing aliovalent Sr-doping content, leading to reduction of the Madelung energy, resulting in the bonding energy decrease and unit-cell dilation. Interestingly, the dilatometric behavior of the higher Sr-doping content, $x = 0.75$, appears to be counter-intuitive, which seems not to be in agreement with what is expected on the basis of ionic sizes. However, the different trend observed in the $La_{0.25}Sr_{0.75}Co_{0.5}Mn_{0.5}O_{3-\delta}$ sample means a different mechanism. From the calculated results, we know that, for $x > 0.5$, the extra holes introduced by Sr tend to be injected into the O sublattice;[31] therefore, a different mechanism operates in $La_{0.25}Sr_{0.75}Co_{0.5}Mn_{0.5}O_{3-\delta}$ to decrease the TECs in contact with $La_{0.5}Sr_{0.5}Co_{0.5}Mn_{0.5}O_{3-\delta}$.

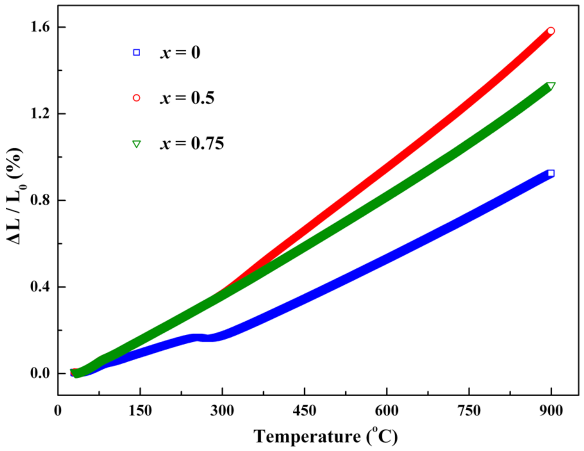

Figure 6. Thermal expansion behaviors of $La_{1-x}Sr_xCo_{0.5}Mn_{0.5}O_{3-\delta}$ ($x = 0$, 0.5, and 0.75) recorded in air.

A mixture of LSCM and SDC in a weight ratio of 1:1 was milled and calcined at 1000 °C for 12 h in air. The chemical compatibility of LSCM with SDC is presented in Figure 7. XRD results demonstrate that no new identifiable peak or obvious diffraction peak shift could be observed, thus indicating the absence of an observable reaction and confirming excellent chemical compatibility between our investigated electrode and electrolyte materials.

Electrochemical Properties. Figure 8 demonstrates the electrical conductivities of the LSCM samples measured by the Van der Pauw four-probe dc method. As can be seen from Figure 8a, the maximum dc conductivities of the LSCM series are 41.4, 140.5, and 204.2 S cm^{-1} for the samples of $x = 0$, 0.5, and 0.75 at 850 °C, respectively. The electrical conductivity is significantly enhanced after the substitution of Sr on the La sites. Aliovalent substitution on the A site introduces mixed-

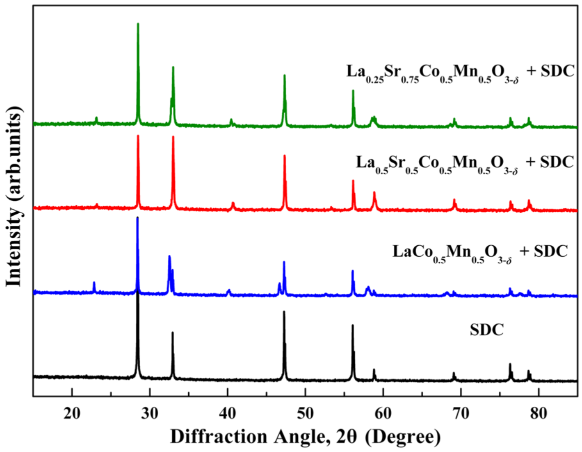

Figure 7. XRD profiles of a mixture of $La_{1-x}Sr_xCo_{0.5}Mn_{0.5}O_{3-\delta}$ ($x = 0$, 0.5, and 0.75) and SDC electrolyte material after being fired at 1000 °C for 12 h. The XRD pattern of a pure SDC electrolyte is also presented for comparison.

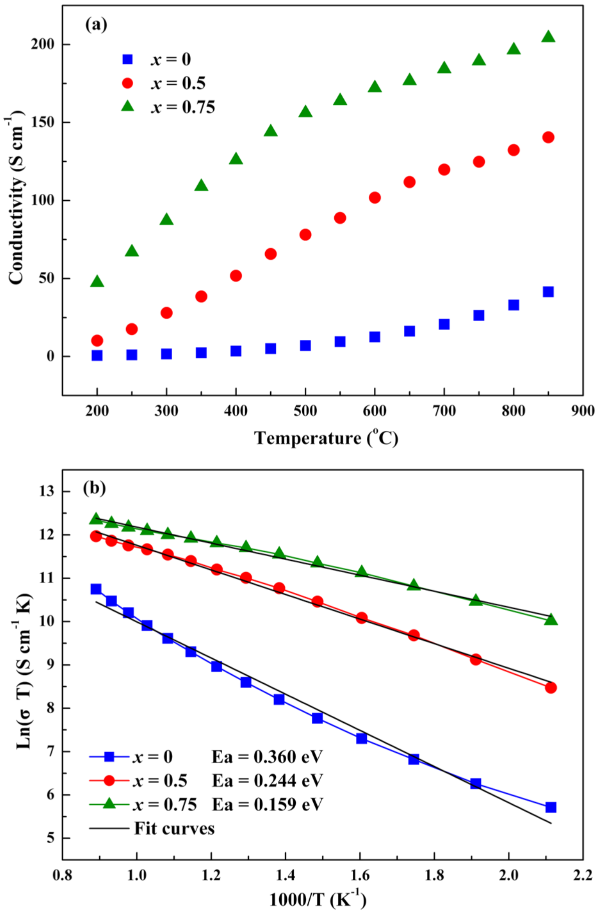

Figure 8. (a) Temperature dependence of the dc conductivity of $La_{1-x}Sr_xCo_{0.5}Mn_{0.5}O_{3-\delta}$ ($x = 0$, 0.5, and 0.75) in air and (b) variations of $\ln(\sigma T)$ as a function of the reciprocal of the absolute temperature in air.

valence states of the transition-metal ions on the B sites, as has been provided through our first-principles-calculated results above. However, the dc conductivity of the LSCM series is slightly lower than that of the LSC,[39] $La_{1-x}Sr_xMnO_3$,[40,41] and $La_{0.8}Sr_{0.2}Co_{0.17}Mn_{0.83}O_3$[41] compounds. Nevertheless, it has been established that MIEC perovskite-type cathode materials should have electrical conductivity as high as ~100 S cm^{-1} to be utilized in practice.[5] From this viewpoint, our investigated Sr-doped LCMO possesses high enough electrical conductivity to fulfill the conventional applications. An almost linear relationship between $\ln(\sigma T)$ and $1000/T$ has been observed in Figure 8b. The apparent activation energies (E_a) were obtained from the linear fit of the Arrhenius curves. The tendency of E_a values for the LSCM family, ($x = 0$; $E_a = 0.360$ eV) < ($x = 0.5$; $E_a = 0.205$ eV) < ($x = 0.75$; $E_a = 0.159$ eV), coincides with that of the dc conductivity. It has been well-known that small-polaron hopping is a thermally activated process and that the conductivity of the small polaron increases with temperature. All of the samples exhibit thermally activated semiconducting behavior over the whole temperature interval, which is consistent with the small-polaron-hopping mechanism.[42]

The typical SEM micrograph of the cross section of $L_{0.25}S_{0.75}CMO|SDC|L_{0.25}S_{0.75}CMO$ is displayed in Figure 9a. The corresponding EDS mapping is also given in Figure 9b. Obviously, spongelike cathode powders are homogeneously distributed and well-connected with the electrolyte. Figure 9c depicts the magnified cathode layer, in which the particles are loosely connected and many large-pore channels are irregularly distributed throughout the grains. The size of the pores is estimated to be ca. 0.5−1.0 μm, and the diameter of the particles is approximately 500 nm. Such a cathode microstructure is believed to be beneficial to decreasing the polarization resistance; thus, an enhancement in the electrochemical performance can be expected.

The cathode performance is also evaluated by impedance spectroscopy measured in air, which is performed on a LSCM|SDC|LSCM symmetrical cell configuration. All of the Nyquist plots (see Figure 10) were moved to the origin of the Z' axis after subtraction of the series resistance in order to compare the cathode polarization processes under different temperatures. As can be seen in Figure 11, the polarization resistances are remarkably improved after replacement of La with Sr, implying that a better oxygen ionic conductivity is obtained because of aliovalent substitution. For these data, the apparent activation energies (E_a) for the oxygen reduction process of 116, 134, and 140 kJ mol^{-1} were determined for the LSCM|SDC|LSCM half-cell with $x = 0$, 0.5, and 0.75 respectively. These values are similar to $LaNi_{0.6}Fe_{0.4}O_3$-based (133 kJ mol^{-1}) and a little lower than $La_{0.8}Sr_{0.2}MnO_3$-based (165 kJ mol^{-1}) cathode materials with the same SDC half-cell configuration.[43] The E_a calculated for the cathode process would suggest that there may be different ORR mechanisms in LSCM. On the basis of our theoretical investigations above, we attributed the enhancement from $x = 0$ to 0.5 not only to even more Co/Mn disorder but also to electron-deficient substitution, both of which promote the oxygen vacancy formation, while the enhancement from $x = 0.5$ to 0.75 mainly originated from the Sr electron-deficient substitution. Quantitatively, the polarization resistances of the LSCM series are about 0.041, 0.027, and 0.022 Ω cm^2 at 850 °C for the samples of $x = 0$, 0.5 and 0.75, respectively. Sr doping clearly improves oxygen transport in LSCM so that the ionic conductivity is comparable to that of $Sr_2Fe_{1.5}Mo_{0.5}O_{6-\delta}$ at 800 °C.[13] This consequence is in excellent agreement with those predicted results. Meanwhile, the R_p values of the LSCM series are much lower than those of LSC,[39] $La_{1-x}Sr_xMnO_3$,[40,41] and $La_{0.8}Sr_{0.2}Co_{0.17}Mn_{0.83}O_3$[41] as electrode materials for IT-SOFCs. Therefore, the LSCM system possesses much potential preponderance for practical application as a cathode material of IT-SOFCs.

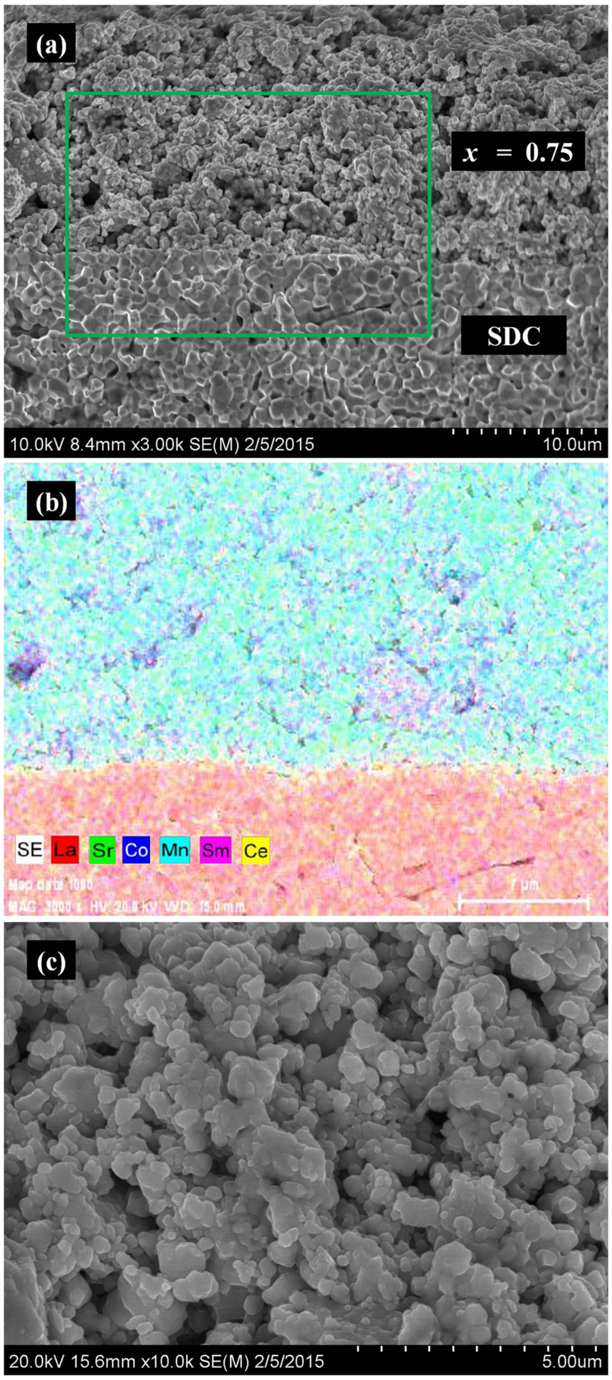

Figure 9. (a) Cross-sectional SEM image of a symmetrical fuel cell of $L_{0.25}S_{0.75}CMO|SDC|L_{0.25}S_{0.75}CMO$. (b) Corresponding EDS mapping. (c) Micrograph of the $L_{0.25}S_{0.75}CM$ cathode layer.

4. CONCLUSION

In this paper, for $La_{1-x}Sr_xCo_{0.5}Mn_{0.5}O_{3-\delta}$ ($x = 0$, 0.5, and 0.75) perovskites, theoretical and experimental efforts were combined

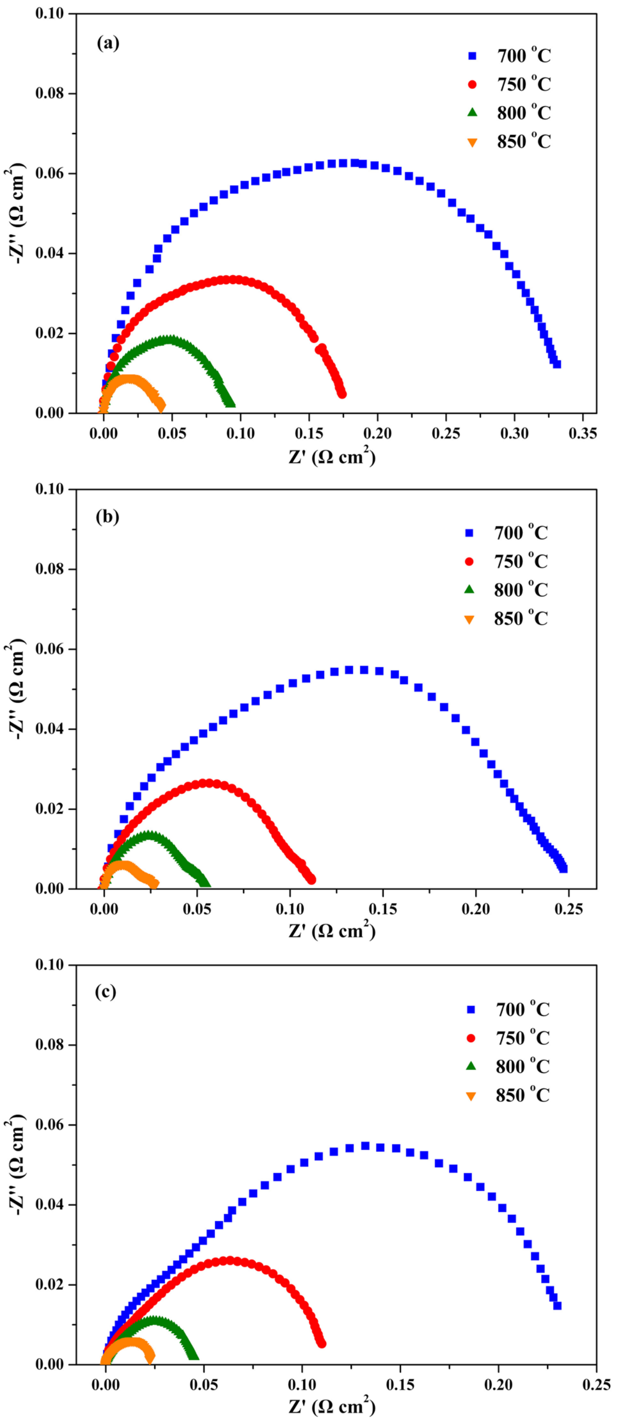

Figure 10. Comparison of impedance spectra among different doping contents in air from 700 to 850 °C: (a) $x = 0$; (b) $x = 0.5$; (c) $x = 0.75$.

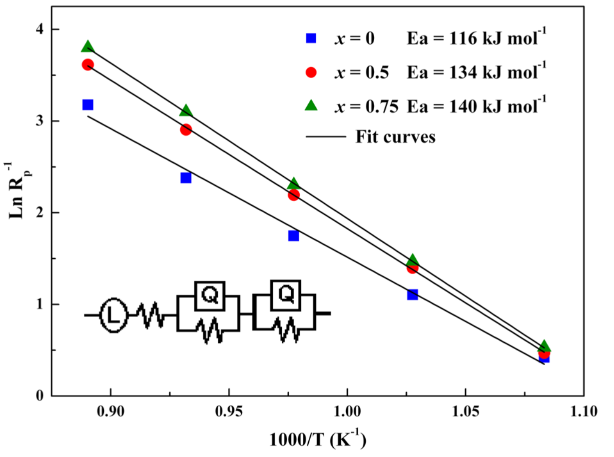

Figure 11. Arrhenius plots for LSCM|SDC|LSCM. An equivalent electrical circuit is shown in the inset.

to explore the effects of the degree of cation disorder and electron-deficient substitution on the oxygen vacancy formation and their influences on the electrochemical properties. First, cation ADs were found to facilitate the oxygen vacancy formation by first-principles calculations. Simultaneously, adding Sr facilitated ADs, which not only decreased the oxygen vacancy formation energy but promoted multivalent states of B-site ions. We also obtained two hole injection steps with the concentration increase of Sr in the LSCM family. Second, a series of LSCM perovskites were synthesized, and their electrochemical properties were comprehensively characterized as cathode materials. Herein, the Sr-doping content of $x = 0.75$ in LSCM features a number of interesting properties that account for the observed performance: it exhibits much higher electronic conductivities and the lowest electrode polarization resistances with the SDC electrolyte over the whole operating temperature range. It is worth noting that the whole LSCM system is testified to be sufficient to fulfill the practical application. Therefore, LSCM can be a good candidate for IT-SOFC cathode materials.

■ ASSOCIATED CONTENT

Ⓢ Supporting Information

Structures, oxygen vacancies, XRD patterns, Rietveld refinement, *M*−*H* hysteresis loops, and bond lengths and angles. This material is available free of charge via the Internet at http://pubs.acs.org.

■ AUTHOR INFORMATION

Corresponding Authors

*E-mail: lxjuan@ciac.ac.cn.
*E-mail: mengtiantang0527@hotmail.com.

Author Contributions

$^{\perp}$All of the theoretical calculations were carried out by N.Y.

Notes

The authors declare no competing financial interest.

■ ACKNOWLEDGMENTS

This work was supported by the National Natural Science Foundation of China under Grants 51002148 and 20921002 and the Natural Scientific Foundation of Jilin Province under Grant 20130101016JC.

■ REFERENCES

(1) Tao, S.; Irvine, J. T. S. *Nat. Mater.* **2003**, *2*, 320−323.
(2) Steele, B. C. H.; Heinzel, A. *Nature* **2001**, *414*, 345−352.
(3) Fergus, J. W. *Mater. Sci. Eng., A* **2005**, *397*, 271−283.
(4) Tamimi, M. A.; Mclntosh, S. *J. Mater. Chem. A* **2014**, *2*, 6015−6026.
(5) Yuste, M.; Pérez-Flores, J. C.; Paz, J. R.; Azcondo, M. T.; García-Alvarado, F.; Amador, U. *Dalton Trans.* **2011**, *40*, 7908−7915.
(6) Shao, Z. P.; Haile, S. M. *Nature* **2004**, *431*, 170−173.
(7) Liu, B.; Chen, X. B.; Dong, Y. L.; Mao, S. S.; Cheng, M. J. *Adv. Energy Mater.* **2011**, *1*, 343−346.

(8) Navarro, J.; Balcells, L.; Sandiumenge, F.; Bibes, M.; Roig, A.; Martínez, B.; Fontcuberta, J. *J. Phys.: Condens. Matter* **2001**, *13*, 8481−8488.
(9) King, G.; Woodward, P. M. *J. Mater. Chem.* **2010**, *20*, 5785−5796.
(10) Muñoz-García, A. B.; Pavone, M.; Carter, E. A. *Chem. Mater.* **2011**, *23*, 4525−4536.
(11) Pavone, M.; Ritzmann, A. M.; Carter, E. A. *Energy Environ. Sci.* **2011**, *4*, 4933−4937.
(12) Kobayashi, K. I.; Kimura, T.; Sawada, H.; Terakura, K.; Tokura, Y. *Nature* **1998**, *395*, 677−680.
(13) Liu, Q.; Dong, X. H.; Xiao, G. L.; Zhao, F.; Chen, F. L. *Adv. Mater.* **2010**, *22*, 5478−5482.
(14) Muñoz-García, A. B.; Bugaris, D. E.; Pavone, M.; Hodges, J. P.; Huq, A.; Chen, F. L.; zur Loye, H.-C.; Carter, E. A. *J. Am. Chem. Soc.* **2012**, *134*, 6826−6833.
(15) Bull, C. L.; Gleeson, D.; Knight, K. S. *J. Phys.: Condens. Matter* **2003**, *15*, 4927−4936.
(16) Ritzmann, A. M.; Muñoz-García, A. B.; Pavone, M.; Keith, J. A.; Carter, E. A. *Chem. Mater.* **2013**, *25*, 3011−3019.
(17) Dudarev, S. L.; Botton, G. A.; Savrasov, S. Y.; Humphreys, C. J.; Sutton, A. P. *Phys. Rev. B* **1998**, *57*, 1505−1509.
(18) Blochl, P. E. *Phys. Rev. B* **1994**, *50*, 17953−17979.
(19) Kresse, G.; Joubert, D. *Phys. Rev. B* **1999**, *59*, 1758−1775.
(20) Perdew, J. P.; Burke, K.; Ernzerhof, M. *Phys. Rev. Lett.* **1996**, *77*, 3865−3868.
(21) Monkhorst, H. J.; Pack, J. D. *Phys. Rev. B* **1976**, *13*, 5188−5192.
(22) Blochl, P. E.; Jepsen, O.; Andersen, O. K. *Phys. Rev. B* **1994**, *49*, 16223−16233.
(23) Bader, R. F. W. *Atoms in Molecules: A Quantum Theory*; Oxford University Press: New York, 1994.
(24) Tang, W.; Sanville, E.; Henkelman, G. *J. Phys.: Condens. Matter* **2009**, *21*, 084204−084211.
(25) Pérez-Flores, J. C.; Pérez-Coll, D.; García-Martín, S.; Ritter, C.; Mather, G. C.; Canales-Vázquez, J.; Gálvez-Sánchez, M.; García-Alvarado, F.; Amador, U. *Chem. Mater.* **2013**, *25*, 2484−2494.
(26) Huang, W.; Shuk, P.; Greenblatt, M. *Solid State Ionics* **1997**, *100*, 23−27.
(27) Toby, B. H. *J. Appl. Crystallogr.* **2001**, *34*, 210−213.
(28) Chen, X.; Jiang, S. P. *J. Mater. Chem. A* **2013**, *1*, 4871−4878.
(29) Lv, S. H.; Liu, X. J.; Li, H. P.; Han, L.; Wang, Z. C.; Meng, J. *J. Comput. Chem.* **2012**, *33*, 1433−1439.
(30) Pavone, M.; Muñoz-García, A. B.; Ritzmann, A. M.; Carter, E. A. *J. Phys. Chem. C* **2014**, *118*, 13346−13356.
(31) Saitoh, T.; Bocquet, A. E.; Mizokawa, T.; Namatame, H.; Fujimori, A.; Abbate, M.; Takeda, Y.; Takano, M. *Phys. Rev. B* **1995**, *51*, 13942−13951.
(32) Milenov, T. I.; Rafailov, P. M.; Abrashev, M. V.; Nikolova, R. P.; Nakatsuka, A.; Avdeev, G. V.; Veleva, M. N.; Dobreva, S.; Yankova, L.; Gospodinov, M. M. *Mater. Sci. Eng., B* **2010**, *172*, 80−84.
(33) Singh, P.; Goodenough, J. B. *J. Am. Chem. Soc.* **2013**, *135*, 10149−10154.
(34) Shannon, R. D. *Acta Crystallogr., Sect. A* **1976**, *32*, 751−767.
(35) Sears, V. F. *Neutron News* **1992**, *3*, 26−37.
(36) Deng, J.; Zhang, L.; Dai, H.; He, H.; Au, C. T. *Ind. Eng. Chem. Res.* **2008**, *47*, 8175−8183.
(37) Eguchi, K.; Setoguchi, T.; Inoue, T.; Arai, H. *Solid State Ionics* **1992**, *52*, 165−172.
(38) Xiao, G.; Liu, Q.; Zhao, F.; Xiao, G.; Zhang, L.; Xia, C.; Chen, F. *J. Electrochem. Soc.* **2011**, *158*, B455−B460.
(39) Gwon, O.; Yoo, S.; Shin, J.; Kim, G. *Int. J. Hydrogen Energy* **2014**, *39*, 20806−20811.
(40) Lee, H. K. *Mater. Chem. Phys.* **2002**, *77*, 639−646.
(41) Bai, Y. H.; Liu, M. F.; Ding, D.; Blinn, K.; Qin, W. T.; Liu, J.; Liu, M. L. *J. Power Sources* **2012**, *205*, 80−85.
(42) Montini, T.; Bevilacqua, M.; Fonda, E.; Casula, M. F.; Lee, S.; Tavagnacco, C.; Gorte, R. J.; Fornasiero, P. *Chem. Mater.* **2009**, *21*, 1768−1774.
(43) Bevilacqua, M.; Montini, T.; Tavagnacco, C.; Fonda, E.; Fornasiero, P.; Graziani, M. *Chem. Mater.* **2007**, *19*, 5926−5936.